Constructing electrostatic self-assembled 2D/2D ultra-thin $ZnIn_2S_4$/protonated g-C_3N_4 heterojunctions for excellent photocatalytic performance under visible light

Hongcen Yang, Ruya Cao, Pengxiao Sun, Jiangmei Yin, Shouwei Zhang*, Xijin Xu*

School of Physics and Technology, University of Jinan, 336 West Road of Nan Xinzhuang, Jinan, 250022, Shandong, PR China

ARTICLE INFO

ABSTRACT

2D/2D ultra-thin $ZnIn_2S_4$/protonated g-C_3N_4 nanocomposites ($ZnIn_2S_4$/pCN) are fabricated by electrostatic self-assembly strategy between negatively charged 2D ultra-thin $ZnIn_2S_4$ nanosheets and 2D protonated g-C_3N_4 nanosheets. The optimized $ZnIn_2S_4$/pCN (5:3) shows excellent photocatalytic activity toward H_2 production ($\tilde{}8601.16\,\mu mol\,g^{-1}\,h^{-1}$) under visible light. In addition, $ZnIn_2S_4$/pCN also exhibits superior visible-light-driven photocatalytic tetracycline degradation efficiency, about ˜4.13 and ˜2.28 times higher than protonated g-C_3N_4 and ultra-thin $ZnIn_2S_4$, respectively. The optimal $ZnIn_2S_4$/pCN (5:3) also has good photostability. The excellent photocatalytic activity of $ZnIn_2S_4$/pCN can be attributed to the unique 2D/2D heterojunctions, which are obtained by electrostatic self-assembly. The intimate interfacial contact and larger contact areas promote the separation and migration of photogenerated carriers, which contribute to the improvement of photocatalytic activity and photostability. Our research on the 2D/2D nanocomposites provides a scalable solution for the research of efficient and active photocatalysts.

1. Introduction

Nowadays, photocatalysis, as a green technology, is recognized as an effective method for the research of renewable energy and effective environmental governance [1–3]. However, the narrow range of photoresponse and the rapid recombination of photogenerated e^- and h^+ are the main problems in photocatalysis [4–6]. So the development of photocatalysts with high efficiency, stability, and ease of production is greatly desired [7,8]. Two-dimensional (2D) g-C_3N_4, as a non-metallic polymeric material, has received much more attention in the area of photocatalysis for its large specific surface area, suitable band positions, excellent thermal and chemical stability, ease of production and environmental friendliness [9–11]. However, g-C_3N_4 still suffers from insufficient utilization of visible light and the rapid recombination of photogenerated carriers, which seriously restrict its practical applications [12,13]. A great deal of strategies have been carried out to improve the photocatalytic performance via the construction of heterojunctions, the doping of metallic and non-metallic materials, the regulation of morphologies and coupling with other semiconductors, etc [14–16]. Among them, the construction of the heterojunction can effectively accelerate the separation and migration of photogenerated carriers, and significantly improve the photocatalytic activities of g-

C_3N_4-based heterostructure composites under visible light [14,17,18].

Layered $ZnIn_2S_4$, as a typical ternary chalcogenide, has attracted wide attention in photocatalysis due to wide visible-light response range, excellent electrical and optical properties, environmental friendliness, and remarkable chemical stability [19–21]. Importantly, $ZnIn_2S_4$ has a suitable bandgap structure, which is conducive to matching with g-C_3N_4 [21–23]. This facilitates the construction of $ZnIn_2S_4$/g-C_3N_4 heterojunction nanocomposites and achieves high-efficiency separation and migration of photogenerated carriers of nanocomposites [24,25]. In the previous reports, 0D/2D $ZnIn_2S_4$/g-C_3N_4 heterojunctions have been synthesized with good visible-light photocatalytic H_2 production [26], in which the small contact surfaces likely mean the serious charge congestions occurred on the contact surfaces [27–29]. Furthermore, the typical 0D materials with a certain size lead to an increase in the transmission distance of photogenerated charges, which result in the poor photogenerated charge separation and transfer as well as reduce the photocatalytic activity of photocatalysts [26,30–32]. Therefore, the 2D/2D ZnInS/g-C_3N_4 heterojunctions are constructed because they own a lot of advantages by comparing with 0D/2D heterojunctions: i) the 2D/2D ZnInS/g-C_3N_4 heterojunctions have intimate interfacial contact and larger contact areas compared with 0D/2D heterojunctions materials, which can provide plentiful

charge transfer channels; ii) photogenerated charges of 2D/2D ZnInS/g-C$_3$N$_4$ heterojunctions have shorter migration distance and time compared with 0D/2D heterojunctions materials [24,32–34]. All of these contribute to excellent stability, high separation and migration rate and efficient photocatalytic activity [12,19]. Some work has been done based on 2D/2D ZnInS/g-C$_3$N$_4$. Wu et al. fabricated Zn$_3$In$_2$S$_6$/fluorinated polymeric carbon nitride photocatalyst through hydrothermal method for photocatalytic H$_2$ production under visible light [23]; Lin et al. displayed the prepared of 2D/2D g-C$_3$N$_4$ @ZnIn$_2$S$_4$ with high-efficiency photocatalytic H$_2$ evolution [24]; Liu et al. constructed 2D/2D ZnIn$_2$S$_4$/g-C$_3$N$_4$ nanostructures by hydrothermal synthesis, which achieved excellent photocatalytic H$_2$ production performance [25]. These 2D/2D ZnInS/g-C$_3$N$_4$ nanocomposites are constructed by hydrothermal method. However, the high temperature and pressure reaction process in hydrothermal method restricts the applications of ZnIn$_2$S$_4$/g-C$_3$N$_4$ nanocomposites in photocatalysis due to the safety issues and higher costs for fabrication of photocatalysts. Herein, the development of a simple, safe and effective preparation method for synthesizing 2D/2D ultra-thin ZnInS/g-C$_3$N$_4$ nanocomposites with impressive photocatalytic properties is necessary.

Based on the above considerations, we constructed ultra-thin ZnIn$_2$S$_4$ and protonated g-C$_3$N$_4$ (2D/2D) nanocomposites via a simple electrostatic self-assembly method, which can make the protonated g-C$_3$N$_4$ nanosheets better combination with ultra-thin ZnIn$_2$S$_4$ to form 2D/2D heterojunctions. The electrostatic self-assembly method to construct 2D/2D ultra-thin ZnIn$_2$S$_4$/protonated g-C$_3$N$_4$ heterojunction nanocomposites is also simple, convenient and inexpensive compared with hydrothermal methods [21,35,36]. The constructed 2D/2D ultra-thin ZnIn$_2$S$_4$/protonated g-C$_3$N$_4$ nanocomposites facilitate the formation of uniform morphologies and more efficient photogenerated charges transfer between heterointerfaces. Herein, the outstanding photocatalytic H$_2$ evolutions of the prepared 2D/2D ultra-thin ZnIn$_2$S$_4$/protonated g-C$_3$N$_4$ heterojunction nanocomposites are also achieved.

2. Experimental section

2.1. Materials

All the chemicals are analytical grade from Sinopharm Chemical Reagent Co., Ltd and used as received without any further purification.

2.2. Synthesis of protonated g-C$_3$N$_4$ nanosheets (pCN)

The pCN was prepared by calcining urea. Firstly, urea in covered crucible was heated to 550 °C for 240 min to obtain bulk g-C$_3$N$_4$. The bulk g-C$_3$N$_4$ was then heated to 500 °C for 120 min for the syntheis of g-C$_3$N$_4$ nanosheets (CNNS). Then, g-C$_3$N$_4$ nanosheets (4 g) was dispersed to HCl aqueous solution (500 mL, 1 mol·L^{-1}) by ultrasonic treatment for 60 min and stirred for another 60 min for the protonation in the acid suspension. The pCN was collected and washed by deionized water to remove HCl until the pH value became 7. Finally, the pCN was dried in a vacuum oven.

2.3. Synthesis of ultra-thin ZnIn$_2$S$_4$ nanosheets

Zn(CH$_3$COO)$_2$·2H$_2$O (3 mmol), InCl$_3$ (6 mmol) and thioacetamide (TAA, 16 mmol) were added into deionized water (500 mL) and stirred for 30 min, and was then heated to 95 °C and maintained 300 min under vigorous stirring. The resulted precipitation was collected, rinsed with deionized water for 2 times and redispersed into 500 mL deionized water. The dispersion was sonicated continuously for 120 min and then centrifuged at 6000 r.p.m. for 5 min to remove aggregations. After that, ultra-thin ZnIn$_2$S$_4$ nanosheets were obtained [21].

2.4. Synthesis of ultra-thin ZnIn$_2$S$_4$/protonated g-C$_3$N$_4$ nanosheets composites (ZnIn$_2$S$_4$/pCN)

Firstly, ZnIn$_2$S$_4$ (100 mg) was dispersed into deionized water (200 mL) by ultrasonic. Then, a certain amount of pCN was was dispersed into deionized water by ultrasonic to obtain a mixed solution (0.5 mg·mL^{-1}). Finally, the pCN suspension was dripped to the ultra-thin ZnIn$_2$S$_4$ solution drop by drop. In the experiment, ZnInS/pCN composites with different mass ratios of ZnIn$_2$S$_4$ and pCN (5:1, 5:2, 5:3, 5:4, 5:5) were synthesized and labeled as ZnIn$_2$S$_4$, ZnIn$_2$S$_4$/pCN (5:1), ZnIn$_2$S$_4$/pCN (5:2), ZnIn$_2$S$_4$/pCN (5:3), ZnIn$_2$S$_4$/pCN (5:4), ZnIn$_2$S$_4$/pCN (5:5), pCN.

2.5. Characterization methods

UV-vis was tested via a Shimadzu UV-2500 spectrophotometer. The structural characteristics and morphologies were obtained by X-ray diffraction (XRD, D/MAX2500 V diffractometer), fourier transform spectrophotometer (FT-IR, Avatar 370, Thermo Nicolet) and X-ray photoelectron spectroscopy (XPS, SCALAB250. using C1s peak at 284.6 eV as standard), scanning electron microscopy (SEM, JEOL JSM-6330 F) and transmission electron microscope (FETEM, JEOL-2100). The PL was measured by Shimadzu RF-6000. Transient photocurrent responses, the electrochemical impedance spectroscopy and Mott-Schottky plots were tested via a three-electrode cell system (CHI660E electrochemical station and 50 mW LED as light source and 1 M Na$_2$SO$_4$ solution as electrolyte). In addition, transient photocurrent responses and Mott-Schottky plots used 1 M Na$_2$SO$_4$ solution as electrolyte, and the electrochemical impedance spectroscopy used the 1 M KOH aqueous solution as the electrolyte.

2.6. Photocatalytic tests

For the photocatalytic hydrogen evolutions, a Xe lamp (300 W) with a cutoff optical filter (400 nm) was used as the visible-light source. The ZnIn$_2$S$_4$/pCN photocatalyst (10 mg) was dispersed in mixed aqueous solution containing 100 mL deionized water and 20 mL TEOA as sacrificial agents. Before irradiation, the reaction system (Beijing Aulight CO., Ltd.) with a gas chromatogram (GC) was pumped to vacuum to ensure an anaerobic condition. The H$_2$ evolution rates of ZnIn$_2$S$_4$/pCN were measured at different irradiation wavelengths with band-pass filters of 365 ± 5, 380 ± 5, 400 ± 5, 420 ± 5, 450 ± 5, 475 ± 5, 500 ± 5, 550 ± 5 and 600 ± 5 nm. The apparent quantum efficiency (AQE) can be obtained from the following equation [37]:

$$AQE[\%] = \frac{\text{number of reacted electrons}}{\text{number of incident photons}} \times 100$$

$$= \frac{\text{number of evolved H}_2 \text{ molecules} \times 2}{\text{number of incident photons}} \times 100$$

The photocatalytic degradation activities were obtained by degrading tetracycline under the visible light irradition (a 500 W Xe lamp with a cutoff filter ($\lambda \geq 420$ nm)). In short, photocatalysts (20 mg) were dispersed to 50 mL of tetracycline aqueous solution (50 mg·L^{-1}). After adsorption-desorption equilibrium in a dark environment, the photocatalytic efficiencies were tested by a UV–vis spectro-photometer (UV-2500, Shimadzu).

3. Results and discussion

The preparation process of ZnIn$_2$S$_4$/pCN nanocomposites is illustrated in Fig. 1A, the negatively charged ZnIn$_2$S$_4$ is slowly added dropwise to the positively charged pCN, and the mixed solution (pH ~4.5) is thoroughly stirred to obtain ZnIn$_2$S$_4$/pCN. Rapid precipitations of ZnIn$_2$S$_4$/pCN nanocomposites are successfully synthesized by electrostatic attraction, which is conducive to large-scale production of the
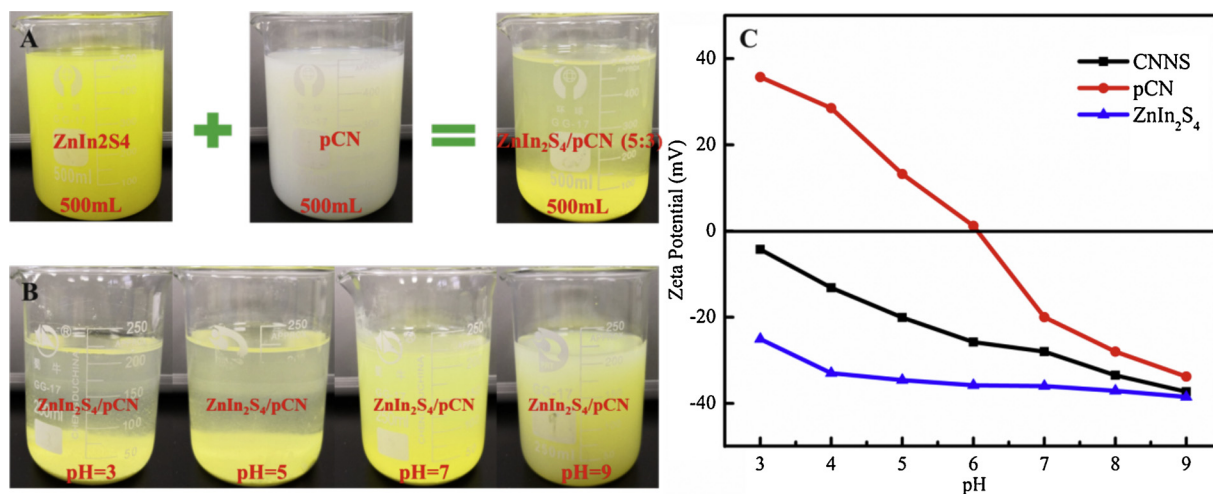
Fig. 1. (A) digital photographs of $ZnIn_2S_4$/pCN nanocomposites solutions, (B) digital photographs of $ZnIn_2S_4$/pCN nanocomposites at different pH, (C) Zeta potential of CNNS, pCN and $ZnIn_2S_4$ at different pH.

$ZnIn_2S_4$/pCN nanocomposites. The feasibility of the method for the preparation of the $ZnIn_2S_4$/pCN nanocomposites is also verified under different pH conditions as shown in Fig. 1B, in which the pCN and $ZnIn_2S_4$ are well mixed at different pH (the pH was adjusted by 0.1 M NaOH and 0.1 M HCl) and allowed to stand for 1 h. The mixture can precipitate quickly under pH ~3 and 5, which means the successful synthesis of the nanocomposites. No precipitations can be found under pH ~7 and 9, which means that the electrostatic interaction between is weakened and completely disappears. Zeta potential (Fig. 1C) is measured to demonstrate the effect of pH. Observed from Fig. 1C, pCN and $ZnIn_2S_4$ hold positive and negative charges when the pH values are below 6, indicating that the pCN and $ZnIn_2S_4$ can be self-assembled by static electricity. When the pH values are above 6, both pCN and $ZnIn_2S_4$ have positive charges. As the pH values increases, less precipitate will be formed, while more pCN and $ZnIn_2S_4$ are still dispersed in the aqueous solution.

Fig. 2A displays the XRD patterns of pCN, $ZnIn_2S_4$ and $ZnIn_2S_4$/pCN nanocomposites with different pCN contents. Two characteristic diffraction peaks of pCN around 12.8° and 27.5° can be clearly identified as (100) and (002) [38,39]. The XRD characteristic diffraction peaks of $ZnIn_2S_4$ correspond to hexagonal crystal structure (JCPDS No. 65-2023, a = b = 3.85 Å, c = 24.68 Å) [21,40]. For the $ZnIn_2S_4$/pCN nanocomposites, a characteristic diffraction peak at ~27.6° belongs to the overlap of the (002) reflection peak of CNNS (27.5°) and the (102) reflection peak of hexagonal $ZnIn_2S_4$ (27.7°), and the characteristic diffraction peak is gradually enhanced with the increase of pCN [41]. Other characteristic diffraction peaks in the $ZnIn_2S_4$/pCN

nanocomposites correspond well to hexagonal $ZnIn_2S_4$ [21]. To further confirm the presence of pCN in the nanocomposites, the FT-IR spectra are tested (Fig. 2B), in which the peaks in the region of 3200–3700 cm^{-1} are ascribed to the N−H and O−H stretching vibration modes of pCN [39,42]. Several strong peaks at 1244, 1319, 1409, 1460, 1573 and 1635 cm^{-1} are attributed to aromatic C−N stretching vibration modes and C=N stretching vibration modes [16,27,43]. The characteristic vibration of triazine rings at 812 cm^{-1} is also observed [31,44]. These results are also found in the $ZnIn_2S_4$/pCN nanocomposites, further proving the existence of pCN in the nanocomposites. In addition, two peaks at 1384 and 1631 cm^{-1} belong to surface absorbed water rmolecules, and the hydroxyl groups are observed in $ZnIn_2S_4$, which also exist for the $ZnIn_2S_4$/pCN nanocomposites [21]. These results indicate the successful synthesis of the $ZnIn_2S_4$/pCN nanocomposites.

The UV–vis diffuse reflection spectra in Fig. 3(A) show that the absorption of pCN ranges from the UV to the visible light (~450 nm). For $ZnIn_2S_4$, the absorption edge of is ~ 570 nm, displaying a wide visible light absorption range. The absorption edges of $ZnIn_2S_4$/pCN (5:1), $ZnIn_2S_4$/pCN (5:2), $ZnIn_2S_4$/pCN (5:3), $ZnIn_2S_4$/pCN (5:4) and $ZnIn_2S_4$/pCN (5:5) slightly shift to longer wavelength in comparison with pCN. The red shift means that $ZnIn_2S_4$/pCN composites can absorb more visible light and provide more carriers, which improves the photocatalytic performance of composites. The values of energy bandgaps calculated via the Kubelka-Munk method (the Kubelka-Munk formula: $\alpha h\nu = A(h\nu - E_g)^{n/2}$, $n_{direct\ transition} = 1$ and $n_{indirect\ transition} = 4$). For pCN and $ZnIn_2S_4$, the n value of 1 is used [16,25]. The values of
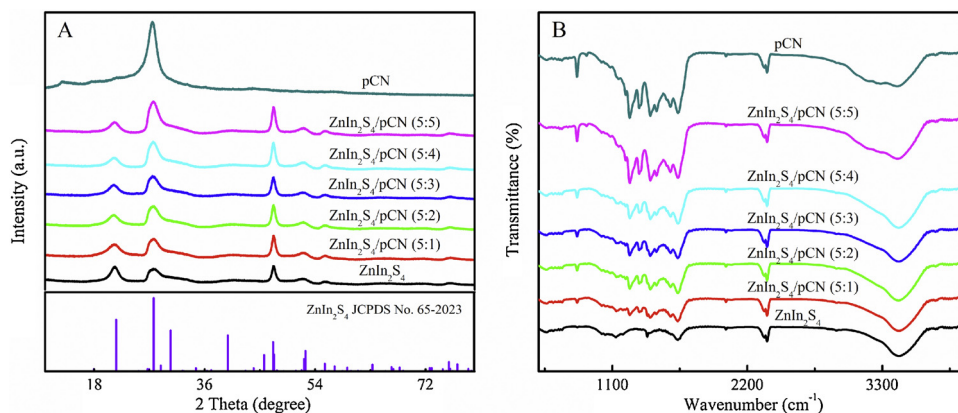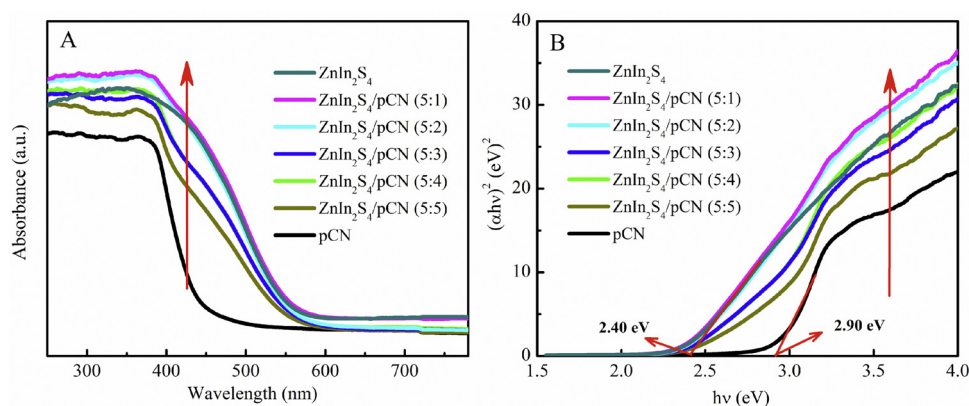

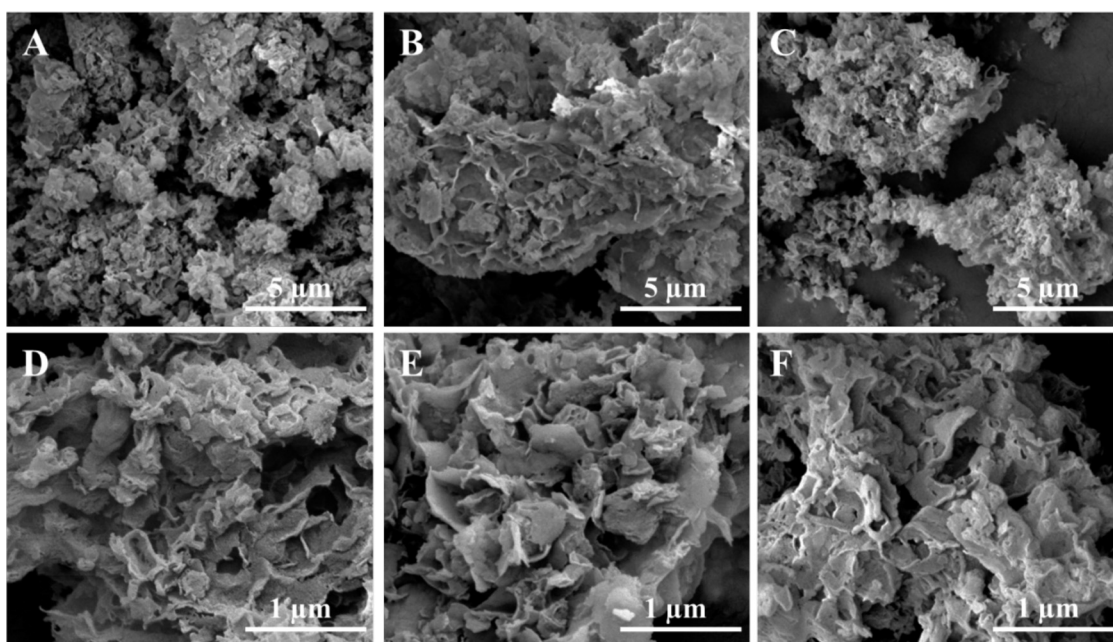**Fig. 2.** (A) XRD and (B) FT-IR patterns of pCN, $ZnIn_2S_4$ and $ZnIn_2S_4$/pCN nanocomposites.

Fig. 3. (A) UV–vis diffuse reflectance spectra of pCN, ZnIn$_2$S$_4$ and ZnIn$_2$S$_4$/pCN nanocomposites, (B) Plot of $(\alpha h\nu)^2$ vs. hν for the band gap energy of pCN, ZnIn$_2$S$_4$ and ZnIn$_2$S$_4$/pCN composites.

energy band-gaps (Fig. 3(B)) for ZnIn$_2$S$_4$, ZnIn$_2$S$_4$/pCN (5:1), ZnIn$_2$S$_4$/pCN (5:2), ZnIn$_2$S$_4$/pCN (5:3), ZnIn$_2$S$_4$/pCN (5:4), ZnIn$_2$S$_4$/pCN (5:5) and pCN are ~2.40, ~2.51, ~2.58, ~2.65, ~2.77, ~2.85 and ~2.90 eV, respectively. The suitable band gap and red shift can improve the visible-light harvesting ability of pCN, which is beneficial to enhance the H$_2$ generation activity [25,27].

Fig. 4A and D show that the pCN is a three-dimensional (3D) layered structure composed of many ultra-thin 2D nanosheets. The SEM images in Fig. 4C and F indicate that the ZnIn$_2$S$_4$ hold the features of ultra-thin 2D nanosheets. Figure S1 displays the TEM images of pure pCN and ZnIn$_2$S$_4$. The pCN (Figure S1A and B) presents layered structure. Besides, the ZnIn$_2$S$_4$ (Figure S1C and D) exhibit the features of ultra-thin 2D nanosheets. In addition, the HRTEM image (Figure S1D) of pure ZnIn$_2$S$_4$ clearly shows the lattice spacing of ZnIn$_2$S$_4$, which is ~0.32 nm, and this corresponds to the (102) crystal plane. This is consistent with the results of the SEM. In addition, ZnIn$_2$S$_4$/pCN (5:3) (Fig. 4B and E) is also composed of 2D nanosheets, meaning that the morphologies of ZnIn$_2$S$_4$ and pCN will not change during the combination of ZnIn$_2$S$_4$/pCN (5:3). TEM images (Fig. 5A and B) of ZnIn$_2$S$_4$/ pCN (5:3) display that the ZnIn$_2$S$_4$ nanosheets are tightly immobilized on the pCN nanosheets through the electrostatic self-assembly method, which can be further proved by STEM (Fig. 5C). HRTEM image (Fig. 5B) of 2D/2D

ZnIn$_2$S$_4$/pCN (5:3) clearly shows the existence of the 2D/2D interface, where the lattice spacing (~0.32 nm) represents the (102) crystal plane of ZnIn$_2$S$_4$ [21,24]. EDS image in Figure S2 prove the existence of C, N, Zn, In and S elements for ZnIn$_2$S$_4$/pCN (5:3), and the elemental mappings (Fig. 5C) present the uniform distributions of these elements.

Furthermore, the elements to form pCN nanosheets and ZnIn$_2$S$_4$ nanosheets are evenly distinguished in the observed areas from the elemental mappings, which can also prove the integrity of pCN and ZnInS, and the formation of intimate 2D/2D heterostructure in a face-to-face way. The formed 2D/2D architecture greatly improves the separation of photogenerated charges and migration efficiency, which are beneficial to enhance the photocatalytic activities of nanocomposites [23]. Atomic force microscopy (AFM) was used to estimate the thickness of 2D ZnIn$_2$S$_4$ nanosheets and 2D pCN nanosheets. As shown in Figure S3, the typical thickness of 2D ZnIn$_2$S$_4$ nanosheets is ~1.93 nm, and the thickness of 2D pCN nanosheets is ~1.38 nm. In addition, the AFM of ZnIn$_2$S$_4$/pCN (5:3) displays two nanosheets with different thicknesses, corresponding to the thickness of ZnIn$_2$S$_4$ and pCN, respectively. This means the successful synthesis of ZnIn$_2$S$_4$/pCN (5:3) nanocomposite. All of these also prove that both pCN and ZnIn$_2$S$_4$ are ultra-thin nanosheets structures. The ultra-thin nanosheets structures mean that the photogenerated carriers have shorter migration distance,

Fig. 4. SEM images of pCN (A and D), ZnIn$_2$S$_4$/ pCN (5:3) (B and E), ZnIn$_2$S$_4$ (C and F).
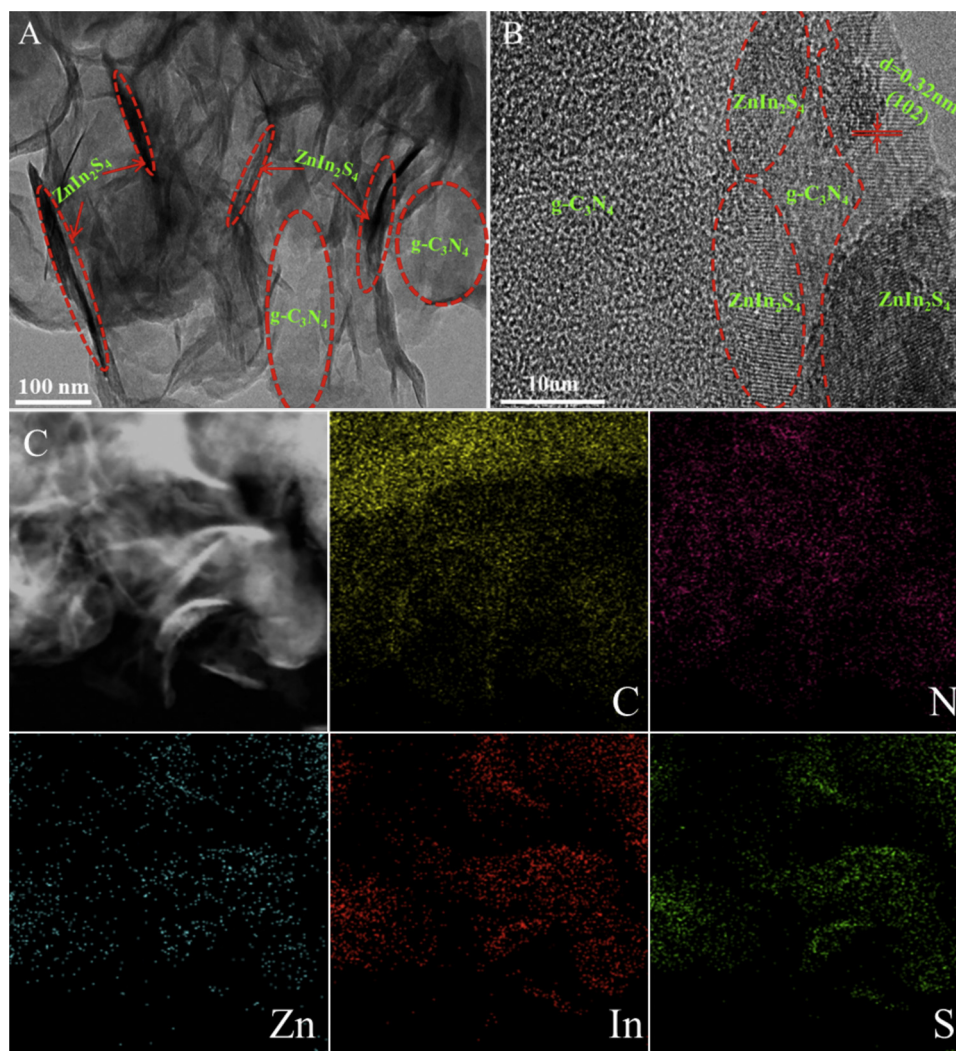
Fig. 5. TEM (A and B) and elemental mapping (C) of $ZnIn_2S_4/$ pCN (5:3).
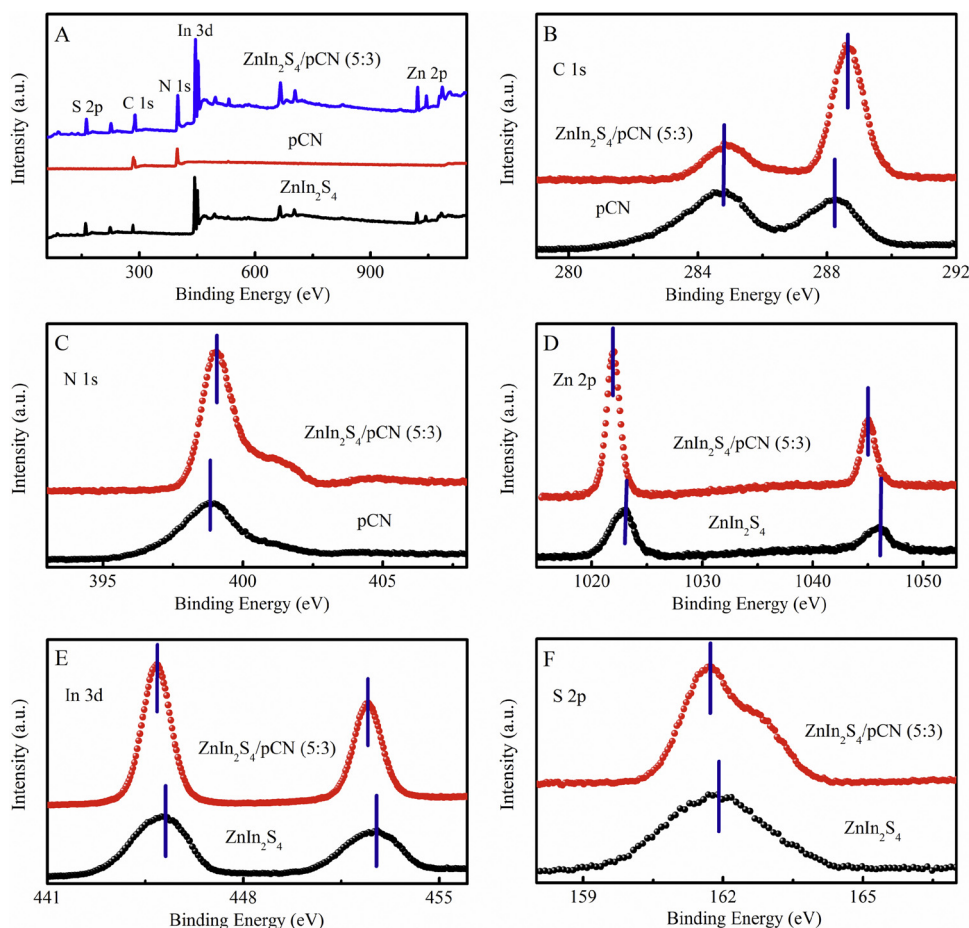
improve the migration efficiency of the photogenerated carriers and contribute to the improvement of the photocatalytic performance.

XPS survey spectra of pCN, $ZnIn_2S_4$/pCN (5:3) and $ZnIn_2S_4$ in Fig. 6A further present the existence of C, N in pCN, Zn, In, S, C, and N in $ZnIn_2S_4$/pCN (5:3) nanocomposite, and Zn, In, S in $ZnIn_2S_4$. The C 1s spectra of $ZnIn_2S_4$/pCN (5:3) and CNNS in Fig. 6B show the characteristic peaks at ˜284.81 eV and ˜288.56 eV, which can be attributed to the sp2-bonds of graphitic carbon (C−C, C═C) and defect-containing sp2-bonded carbon (N−C═N), respectively [25,30]. The peak binding energies of N 1s (Fig. 6C) at ˜399.06 eV is derived from sp^2-hybridized N atoms (C═N−C) [11,45,46]. In addition, the peaks of C 1s and N 1s in the $ZnIn_2S_4$/pCN (5:3) nanocomposite shift to higher binding energies as compared to pCN. Two peaks at ˜1022.06 and 1045.06 eV are observed for Zn 2p spectrum in $ZnIn_2S_4$, corresponding to the Zn $2p_{3/2}$ and Zn $2p_{1/2}$, respectively (Fig. 6D) [47]. After combined with pCN, the peaks of Zn 2p in $ZnIn_2S_4$/pCN (5:3) display lower binding energies as compared to $ZnIn_2S_4$ (Fig. 6D) [19,21]. The binding energies of In 3d in Fig. 6E at ˜444.91 and ˜452.46 eV can be assigned to In $3d_{5/2}$ and In $3d_{3/2}$, respectively [48]. The peak binding energies of ˜161.71 eV (Fig. 6F) is attributed to S 2p [21,49,50]. Correspondingly, peaks of In 3d and S 2p in the $ZnIn_2S_4$/pCN (5:3) nanocomposite also shift towards the lower binding energies in comparison with pure $ZnIn_2S_4$. Compared with pure $ZnIn_2S_4$, the lower binding energies of Zn 2p, In 3d and S 2p in the $ZnIn_2S_4$/pCN (5:3) nanocomposite are observed; while the peaks of C 1s and N 1s in the $ZnIn_2S_4$/pCN (5:3) nanocomposite have higher

binding energies compared with pure g-C_3N_4. These can be attributed to partial electron transfers from pCN to $ZnIn_2S_4$, i.e., the decrease (increase) of the electron density of $ZnIn_2S_4$ (pCN) leads to the enhancement (reduction) of the binding energies of Zn 2p, In 3d and S 2p (C 1s and N 1s), which further confirms the existence of electronic interactions between pCN and $ZnIn_2S_4$, promoting the separation and migration of photogenerated carriers [15,41]. The XPS results indicate the existence of the strong interfacial coupling effect between pCN and $ZnIn_2S_4$, which can promote the separation and migration of photogenerated carriers, and further improve the photocatalytic performance of $ZnIn_2S_4$/pCN (5:3) [15,51]. As shown in Figure S4, the EPR of $ZnIn_2S_4$/pCN (5:3) shows a Lorentzian line in the magnetic field between 3490 and 3540 G. The sharp EPR signal of $ZnIn_2S_4$/pCN (5:3) indicates the existence of defects in the nanocomposites. It is well known that defect-rich structure facilitates an increase in the number of active sites and provides more efficient site for photocatalytic H_2 evolution. In addition, defect engineering can improve the spectral response and photogenerated carriers separation and transfer efficiency of the photocatalyst, thereby improving the photocatalytic performance of the photocatalysts. So this is the another reason for the improvement of photocatalytic activity and photostability of the $ZnIn_2S_4$/pCN.

Photocatalytic H_2 production results in Fig. 7A displays that the productions of cumulative H_2 increase with time over pure pCN, $ZnIn_2S_4$ and $ZnIn_2S_4$/pCN. Within 4 h irradiation, the amounts of H_2 generations are 319, 15,008, 19,021, 21,038, 34,404, 28,970,
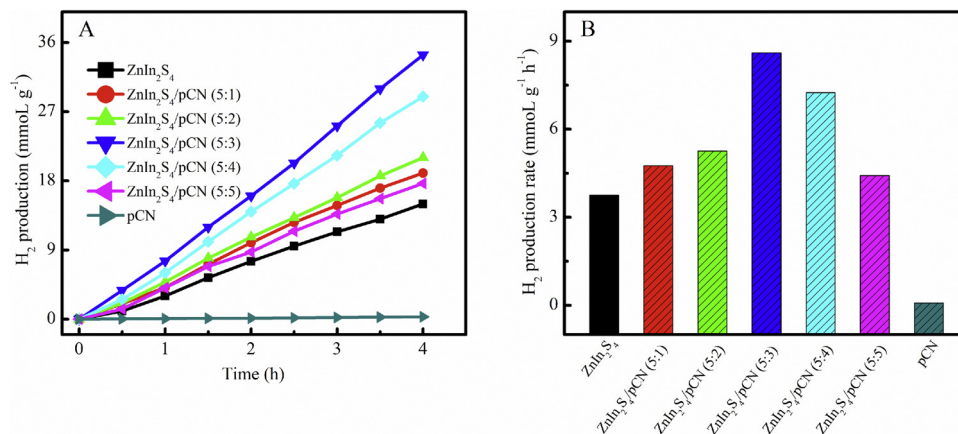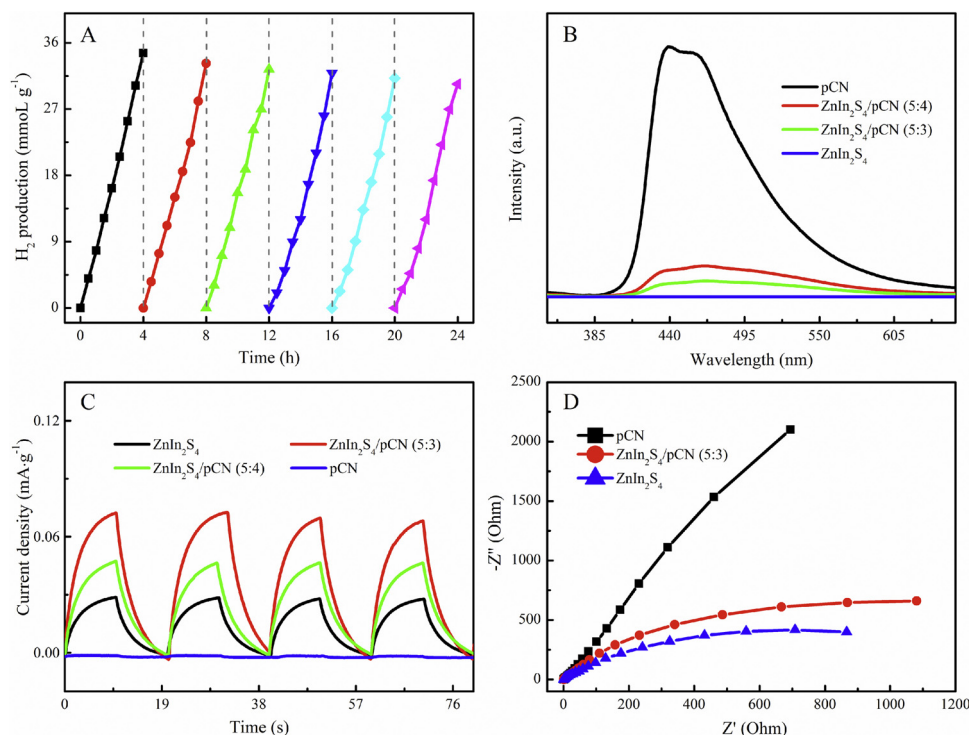
Fig. 6. (A) The XPS survey spectra of pCN, $ZnIn_2S_4/pCN$ (5:3) and $ZnIn_2S_4$; (B) and (C) high resolution spectra of C 1s and N 1s for pCN and $ZnIn_2S_4/pCN$ (5:3); (D), (E) and (F) high resolution spectra of Zn 2p, In 3d and S 2p for $ZnIn_2S_4$ and $ZnIn_2S_4/pCN$ (5:3).

17,676 $\mu mol \cdot g^{-1}$ for CNNS, $ZnIn_2S_4$, $ZnIn_2S_4/pCN$ (5:1), $ZnIn_2S_4/pCN$ (5:2), $ZnIn_2S_4/pCN$ (5:3), $ZnIn_2S_4/pCN$ (5:4) and $ZnIn_2S_4/pCN$ (5:5), respectively. A linear increasing relationship is presented for the cumulative H_2 with the increasing irradiation time, indicating the stability of the materials under visible light. Fig. 7B shows that the H_2 average production rate of $ZnIn_2S_4/pCN$ (5:3) is ˜8601.16 $\mu mol \cdot g^{-1} \cdot h^{-1}$, which is ˜108 times higher than that for pCN and ˜2.3 times higher than that for $ZnIn_2S_4$. In addition, within 4 h irradiation, the amounts of H_2 generation is 11,897 $\mu mol \cdot g^{-1}$ for $ZnIn_2S_4/g\text{-}C_3N_4$ (5:3) (Figure S5). And the amounts of H_2 generations of $ZnIn_2S_4/pCN$ (5:3) is 34,404 $\mu mol \cdot g^{-1}$, which is ˜2.9 times higher than that for $ZnIn_2S_4/g\text{-}$

C_3N_4 (5:3). From Fig. 7, it can be observed that the photocatalytic H_2 production of pCN is very small and negligible, which is due to the rapid recombination of electrons and holes. Compared with pure pCN, the H_2 productions of $ZnIn_2S_4/pCN$ nanocomposites are greatly improved. Besides, the loading of 2D $ZnIn_2S_4$ on pCN effectively expands the absorption range in visible light region. As shown in Figure S6, $ZnIn_2S_4/pCN$ (5:3) presents the AQE of 0.92% at 400 nm and 0.02% at 600 nm, meaning the well photocatalytic activities in the wavelength range of 600 nm. Notably, excess pCN results in a relative decrease of photocatalytic activities, which can be ascribed to the shielding effects of the active sites on the surface of $ZnIn_2S_4$ caused by the excess pCN.

Fig. 7. (A) Time courses and (B)the average rate of H_2 evolution over pCN, $ZnIn_2S_4$ and $ZnIn_2S_4/pCN$ composites.

Fig. 8. (A) cycling test of photocatalytic H_2 generation of $ZnIn_2S_4$/pCN (5:3), (B) photoluminescence spectra, (C) transient photocurrent responses and (D) electrochemical impedance spectroscopy of pCN, $ZnIn_2S_4$ and $ZnIn_2S_4$/pCN composites under visible light irradiation.

The stabilities of $ZnIn_2S_4$/pCN (5:3) are evaluated, as illustrated in Fig. 8A. After six runs (the reaction time is 24 h), the reduction of photocatalytic H_2 production is negligible. The above results indicate the excellent stabilities $ZnIn_2S_4$/pCN (5:3) photocatalyst for H_2 production, which may be due to the separation and migration of photogenerated carriers between 2D $ZnIn_2S_4$ and 2D pCN as well as high photocatalytic stability of pCN in aqueous media. In addition, the synthesis method of electrostatic self-assembly can make 2D $ZnIn_2S_4$ and 2D pCN more firmly combined, which is also beneficial to improve the stability of the nanocomposite. To verify the stabilities of $ZnIn_2S_4$/pCN (5:3), the photocatalysts after photocatalytic reaction for 8 h were characterized (XRD and XPS). As shown in Figure S7 and Figure S8, compared with the original $ZnIn_2S_4$/pCN (5:3), there is no significant change in $ZnIn_2S_4$/pCN (5:3) after reaction in the XRD and XPS. The results indicate that the obtained $ZnIn_2S_4$/pCN (5:3) heterojunction are stable, and the formation of the heterojunction not only effectively improves the photocatalytic activity of pCN, but also improves the light stability of $ZnIn_2S_4$/pCN.
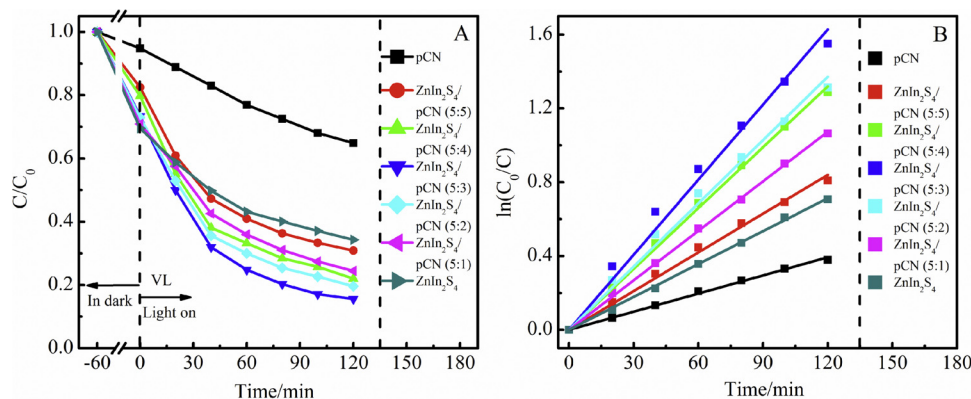
Fig. 8B shows the photoluminescence (PL) spectra of pCN, $ZnIn_2S_4$/pCN (5:3), $ZnIn_2S_4$/pCN (5:4) and $ZnIn_2S_4$ with an excitation wavelength of 335 nm [52]. The pCN displays a strong emission at ˜440 nm, meaning a high recombination rate for photogenerated carriers [53]. The 2D/2D $ZnIn_2S_4$/pCN nanocomposites have lower intensity of peaks than pCN with a order of $ZnIn_2S_4$/pCN (5:3) < $ZnIn_2S_4$/pCN (5:4) < pCN, meaning that the recombination rate of the photogenerated carriers are greatly inhibited in the nanocomposites. Herein, the photocatalytic performance are effectively improved, in consistent with their photocatalytic H_2 productions [54]. In addition, weak PL spectrum of $ZnIn_2S_4$ may be due to the lower amount of photogenerated carriers under the same conditions. Meanwhile, the transient photocurrent responses of pure pCN, $ZnIn_2S_4$/pCN (5:3), $ZnIn_2S_4$/pCN (5:4) and $ZnIn_2S_4$ (Fig. 8C) are measured under visible light irradiation. With the light switched-on and -off cycles, all these samples exhibit obvious transient photocurrent response, and the photocurrent transient response of $ZnIn_2S_4$/pCN (5:3) is greatly higher than $ZnIn_2S_4$/pCN (5:3), pCN and $ZnIn_2S_4$ with a hierarchical order of $ZnIn_2S_4$/pCN

(5:3) > $ZnIn_2S_4$/pCN (5:4) > $ZnIn_2S_4$ > pCN, meaning the effective separation efficiency of the photogenerated carriers for $ZnIn_2S_4$/pCN (5:3). As shown in Fig. 8D, pCN has largest arc and $ZnIn_2S_4$ has a smallest in the Nyquist plot. The arc of $ZnIn_2S_4$/pCN (5:3) is significantly lower than pCN, in order of $ZnIn_2S_4$ < $ZnIn_2S_4$/pCN (5:3) < pCN. This means that the composite of $ZnIn_2S_4$ reduces the charge-transfer resistance of pCN, which promotes the separation and migration of photogenerated carriers [22]. The results of PL, transient photocurrent responses and electrochemical impedance spectroscopies reflect that the 2D/2D $ZnIn_2S_4$/pCN nanocomposites possess have high photogenerated carrier migration and separation efficiency, which is the reason for the improvement of photocatalytic performance [13,23,55].

Degradation experiments of the $ZnIn_2S_4$/pCN nanocomposites for tetracycline (Fig. 9A) were to further test the photocatalytic performance. As expected, the $ZnIn_2S_4$/pCN nanocomposites exhibit higher photocatalytic degradation abilities than both pCN and $ZnIn_2S_4$ with a sequence of $ZnIn_2S_4$/pCN (5:3) > $ZnIn_2S_4$/pCN (5:2) > $ZnIn_2S_4$/pCN (5:4) > $ZnIn_2S_4$/pCN (5:1) > $ZnIn_2S_4$/pCN (5:5) > $ZnIn_2S_4$ > pCN. The degradation of tetracycline with $ZnIn_2S_4$/pCN (5:3)can reach ˜85% within 120 min with visible light irradiation (≥ 420), illustrating the improvement of photocatalytic activities with the loading of 2D $ZnIn_2S_4$ on pCN. However, further increment of pCN on the $ZnIn_2S_4$/pCN nanocomposites leads to the decreased photocatalytic activity, which is consistent with the reason for H_2 production. The rate constants of the photocatalysts for degrading tetracycline are further calculated with the pseudo-first-order model [28].

$$In\left(\frac{C}{C_0}\right) = -Kt$$

K (min^{-1}), C_0 ($mg \cdot L^{-1}$) and C ($mg \cdot L^{-1}$) are the rate constant, the initial concentration of RhB, and the concentration of RhB at time t (min), respectively [53]. The highest degradation rate for tetracycline (Fig. 9B) is 0.01356 min^{-1} for $ZnIn_2S_4$/pCN (5:3), which is ˜4.13, ˜1.94, ˜1.23, ˜1.19, ˜1.51, and ˜2.28 times of pCN (0.0032 min^{-1}), $ZnIn_2S_4$/pCN (5:5) (0.007 min^{-1}), $ZnIn_2S_4$/pCN (5:4) (0.0109 min^{-1}), $ZnIn_2S_4$/

Fig. 9. (A) The photocatalytic activities of the as-prepared photocatalysts (20 mg) for the degradation of tetracycline (50 mg L^{-1}) under visible light irradiation, (B) the rate constants of the as-prepared photocatalysts for the degradation of tetracycline.
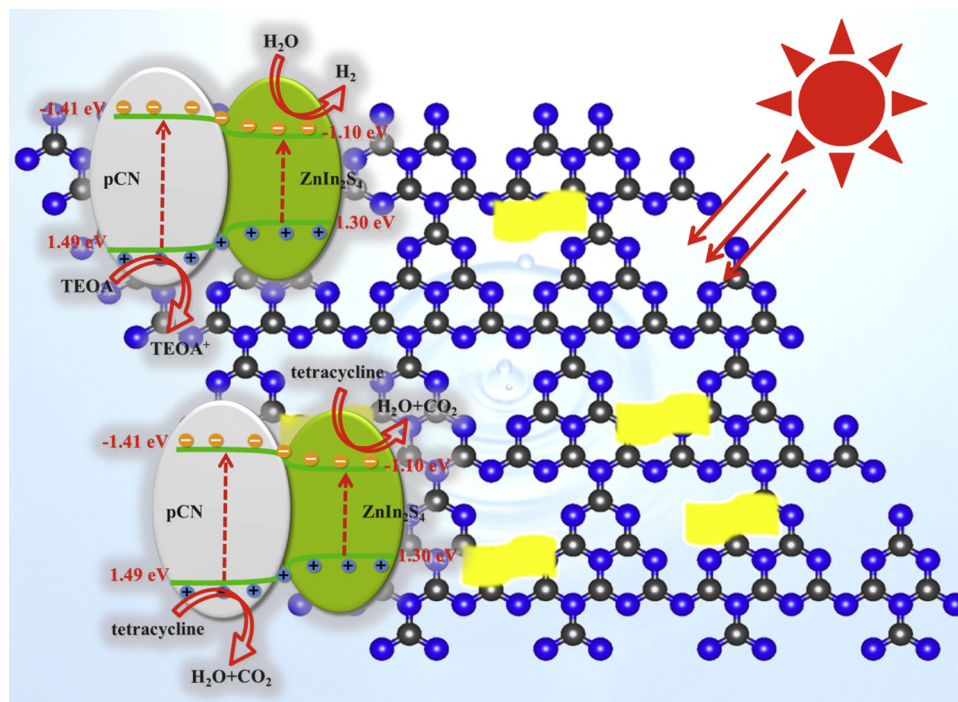
pCN (5:2) (0.0114 min^{-1}), ZnIn$_2$S$_4$/pCN (5:1) (0.0089 min^{-1}) and ZnIn$_2$S$_4$ (0.0059 min^{-1}), respectively.

Based on above conclusions, the proposed mechanism of photogenerated carriers separation and migration for photocatalytic H$_2$ production and photocatalytic degradation has been put forward in the case of the ZnIn$_2$S$_4$/pCN nanocomposites under visible light irradiation (Scheme 1A and B). From Fig. 3B and Figure S9, it is known that the conduction band (CB) and valence band (VB) of ZnIn$_2$S$_4$ are −1.10 and 1.30 eV, the CB and VB of pCN are –1.41 and 1.49 eV. Both ZnIn$_2$S$_4$ and pCN have suitable CB and VB positions, which provide favorable conditions for obtaining the 2D/2D heterojunctions with high-speed charge transfer nanochannels [56,57]. Under the visible light irradiation, both of pCN and ZnIn$_2$S$_4$ are excited to generate a large number of photogenerated carriers. Based on the large CB potential difference between pCN and ZnIn$_2$S$_4$, photogenerated electrons on the CB of pCN are easily transferred to the CB of ZnIn$_2$S$_4$ through the 2D/2D heterojunction interfaces at a high-speed rate of charge transport, which achieves the decomposition of water to produce H$_2$ and the degradation of tetracycline in water. In the reaction of photocatalytic H$_2$ production, these

photogenerated holes on the VB of pCN transfer to the VB of ZnIn$_2$S$_4$. At the same time, these holes are quickly quenched by TEOA, which is used as a sacrificial electron donor. In addition, in the photocatalytic degradation, the photogenerated holes are beneficial for degrading pollutants. It should be noted that the synergy between pCN, ZnIn$_2$S$_4$ and 2D/2D interfaces facilitates the construction of nanochannels for high-speed charge transfer in the 2D/2D system. These nanochannels for fast charge transfer obtained via the formation of 2D/2D heterojunctions greatly shorten the transfer time and the migration distance of photogenerated carriers, significantly improve the transport and separation efficiency of photogenerated carriers, and ultimately lead to significant photocatalytic H$_2$ production performance without the additive Pt cocatalyst and excellent photocatalytic degradation performance for the ZnIn$_2$S$_4$/pCN nanocomposites.

4. Conclusion

In summary, the 2D/2D ZnIn$_2$S$_4$/pCN nanocomposites were successfully prepared via a simple electrostatic self-assembly method,

Scheme 1. Proposed mechanisms of photogenerated charge separation and transfer in the photocatalytic H$_2$ production (A) and photocatalytic degradation (B) for the ZnIn$_2$S$_4$/pCN nanocomposites under visible light irradiation.

achieving plentiful charge transfer channels and strong interaction between ultra-thin $ZnIn_2S_4$ and pCN. This is advantageous for photogenerated electrons on $ZnIn_2S_4$ to migrate to pCN through the 2D/2D heterojunction interface, herein, the separation and migration efficiency of photogenerated carriers are greatly improved, and ultimately leads to a significant enhancement of photocatalytic activity, especially under visible-light-driven. The optimized $ZnIn_2S_4$/pCN (5:3) shows excellent photocatalytic activity toward H_2 production ($\tilde{} 8601.16\,\mu mol \cdot g^{-1} \cdot h^{-1}$) under visible light irradiation, which is $\tilde{} 108$ times of protonated g-C_3N_4 ($79.91\,\mu mol \cdot g^{-1} \cdot h^{-1}$) and $\tilde{} 2.3$ times of $ZnIn_2S_4$ ($3752.01\,\mu mol \cdot g^{-1} \cdot h^{-1}$). $ZnIn_2S_4$/pCN also exhibit superior visible-light-driven photocatalytic tetracycline degradation efficiency, about $\tilde{} 4.13$ and $\tilde{} 2.28$ times of protonated g-C_3N_4 and ultra-thin $ZnIn_2S_4$, respectively. At the same times, cyclic experiment of $ZnIn_2S_4$/pCN (5:3) shows that the nanocomposite has excellent photostability. Therefore, this study is to achieve the simple and efficient method of the unique 2D/2D g-C_3N_4-based nanocomposites with increased photogenerated carriers' lifetime and transfer efficiency, thus improving the photocatalytic activity of 2D/2D g-C_3N_4-based nanocomposites toward practical applications.

Acknowledgements

Appendix A. Supplementary data

Supplementary material related to this article can be found, in the online version, at doi:https://doi.org/10.1016/j.apcatb.2019.117862.

References

[1] N. Guo, Y. Zeng, H. Li, X. Xu, H. Yu, X. Han, Novel mesoporous TiO2@g-C3N4 hollow core@ shell heterojunction with enhanced photocatalytic activity for water treatment and H2 production under simulated sunlight, J. Hazard. Mater. 353 (2018) 80–88.

[2] H. Mou, C. Song, Y. Zhou, B. Zhang, D. Wang, Design and synthesis of porous Ag/ZnO nanosheets assemblies as super photocatalysts for enhanced visible-light degradation of 4-nitrophenol and hydrogen evolution, Appl. Catal. B: Environ. 221 (2018) 565–573.

[3] P. Sun, W. He, H. Yang, R. Cao, J. Yin, C. Wang, X. Xu, Hedgehog-inspired nanostructures for hydrogel-based all-solid-state hybrid supercapacitors with excellent flexibility and electrochemical performance, Nanoscale (2018).

[4] J. Xia, M. Ji, J. Di, B. Wang, S. Yin, Q. Zhang, M. He, H. Li, Construction of ultrathin C3N4/Bi4O5I2 layered nanojunctions via ionic liquid with enhanced photocatalytic performance and mechanism insight, Appl. Catal. B: Environ. 191 (2016) 235–245.

[5] B. Cao, G. Li, H. Li, Hollow spherical RuO2@TiO2@ Pt bifunctional photocatalyst for coupled H2 production and pollutant degradation, Appl. Catal. B: Environ. 194 (2016) 42–49.

[6] P. Sun, C. Wang, W. He, P. Hou, X. Xu, One-step synthesis of 3D network-like NixCo1−xMoO4 porous nanosheets for high performance battery-type hybrid supercapacitors, ACS Sustain. Chem. Eng. 5 (2017) 10139–10147.

[7] M. Zhukovskyi, P. Tongying, H. Yashan, Y. Wang, M. Kuno, Efficient photocatalytic hydrogen generation from Ni nanoparticle decorated CdS nanosheets, ACS Catal. 5 (2015) 6615–6623.

[8] L. Yuan, B. Weng, J.C. Colmenares, Y. Sun, Y.J. Xu, Multichannel charge transfer and mechanistic insight in metal decorated 2D–2D Bi2WO6–TiO2 cascade with enhanced photocatalytic performance, Small 13 (2017) 1702253.

[9] C. Marchal, T. Cottineau, M.G. Méndez-Medrano, C. Colbeau-Justin, V. Caps, V. Keller, Au/TiO2–g-C3N4 nanocomposites for enhanced photocatalytic H2 production from water under visible light irradiation with very low quantities of sacrificial agents, Adv. Energy Mater. 8 (2018) 1702142.

[10] X. Jian, X. Liu, H.-m. Yang, J.-g. Li, X.-l. Song, H.-y. Dai, Z.-h. Liang, Construction of carbon quantum dots/proton-functionalized graphitic carbon nitride nanocomposite via electrostatic self-assembly strategy and its application, Appl. Surf. Sci. 370 (2016) 514–521.

[11] Y.-N. Liu, C.-C. Shen, N. Jiang, Z.-W. Zhao, X. Zhou, S.-J. Zhao, A.-W. Xu, G-C3N4 hydrogen-bonding viologen for significantly enhanced visible-light photocatalytic H2 evolution, ACS Catal. 7 (2017) 8228–8234.

[12] X. She, J. Wu, H. Xu, J. Zhong, Y. Wang, Y. Song, K. Nie, Y. Liu, Y. Yang, M.T.F. Rodrigues, High efficiency photocatalytic water splitting using 2D α-Fe2O3/

g-C3N4 Z-Scheme catalysts, Adv. Energy Mater. 7 (2017) 1700025.

[13] C. Han, Y. Wang, Y. Lei, B. Wang, N. Wu, Q. Shi, Q. Li, In situ synthesis of graphitic-C3N4 nanosheet hybridized N-doped TiO2 nanofibers for efficient photocatalytic H2 production and degradation, Nano Res. 8 (2015) 1199–1209.

[14] J. Fu, J. Yu, C. Jiang, B. Cheng, G-C3N4-based heterostructured photocatalysts, Adv. Energy Mater. 8 (2018) 1701503.

[15] S. Zhang, H. Gao, X. Liu, Y. Huang, X. Xu, N.S. Alharbi, T. Hayat, J. Li, Hybrid 0D–2D nanoheterostructures: in situ growth of amorphous silver silicates dots on g-C3N4 nanosheets for full-spectrum photocatalysis, ACS Appl. Mater. Inter. 8 (2016) 35138–35149.

[16] Y. Li, M. Yang, Y. Xing, X. Liu, Y. Yang, X. Wang, S. Song, Preparation of carbon-rich g-C3N4 nanosheets with enhanced visible light utilization for efficient photocatalytic hydrogen production, Small 13 (2017) 1701552.

[17] L. Zhu, M. Hong, G.W. Ho, Fabrication of wheat grain textured TiO2/CuO composite nanofibers for enhanced solar H2 generation and degradation performance, Nano Energy 11 (2015) 28–37.

[18] C. Wang, K. Guo, H. He, X. Deng, P. Hou, F. Zhuge, X. Xu, T. Zhai, Hierarchical CuCo2O4@nickel-cobalt hydroxides core/shell nanoarchitectures for high-performance hybrid supercapacitors, Sci. Bull. 62 (2017) 1122–1131.

[19] L. Ye, Z. Li, Rapid microwave-assisted syntheses of reduced graphene oxide (RGO)/ZnIn2S4 microspheres as superior noble-metal-free photocatalyst for hydrogen evolutions under visible light, Appl. Catal. B: Environ. 160 (2014) 552–557.

[20] Y.-J. Yuan, D. Chen, J. Zhong, L.-X. Yang, J. Wang, M.-J. Liu, W.-G. Tu, Z.-T. Yu, Z.-G. Zou, Interface engineering of a noble-metal-free 2D-2D MoS2/Cu-ZnIn2S4 photocatalyst for enhanced photocatalytic H2 production, J. Mater. Chem. A 5 (2017) 15771–15779.

[21] M.-Q. Yang, Y.-J. Xu, W. Lu, K. Zeng, H. Zhu, Q.-H. Xu, G.W. Ho, Self-surface charge exfoliation and electrostatically coordinated 2D hetero-layered hybrids, Nat. Commun. 8 (2017) 14224.

[22] W. Chen, T.-Y. Liu, T. Huang, X.-H. Liu, X.-J. Yang, Novel mesoporous P-doped graphitic carbon nitride nanosheets coupled with ZnIn2S4 nanosheets as efficient visible light driven heterostructures with remarkably enhanced photo-reduction activity, Nanoscale 8 (2016) 3711–3719.

[23] Y. Wu, H. Wang, W. Tu, Y. Liu, S. Wu, Y.Z. Tan, J.W. Chew, Construction of hierarchical 2D-2D Zn3In2S6/fluorinated polymeric carbon nitride nanosheets photocatalyst for boosting photocatalytic degradation and hydrogen production performance, Appl. Catal. B: Environ. 233 (2018) 58–69.

[24] B. Lin, H. Li, H. An, W. Hao, J. Wei, Y. Dai, C. Ma, G. Yang, Preparation of 2D/2D g-C3N4 nanosheet@ZnIn2S4 nanoleaf heterojunctions with well-designed high-speed charge transfer nanochannels towards high-efficiency photocatalytic hydrogen evolution, Appl. Catal. B: Environ. 220 (2018) 542–552.

[25] H. Liu, Z. Jin, Z. Xu, Z. Zhang, D. Ao, Fabrication of ZnIn2S4-gC3N4 sheet-on-sheet nanocomposites for efficient visible-light photocatalytic H2-evolution and degradation of organic pollutants, RSC Adv. 5 (2015) 97951–97961.

[26] W. Chen, T.-Y. Liu, T. Huang, X.-H. Liu, J.-W. Zhu, G.-R. Duan, X.-J. Yang, One-pot hydrothermal route to synthesize the ZnIn2S4/g-C3N4 composites with enhanced photocatalytic activity, J. Mater. Sci. 50 (2015) 8142–8152.

[27] W. Xing, C. Li, Y. Wang, Z. Han, Y. Hu, D. Chen, Q. Meng, G. Chen, A novel 2D/2D carbonized poly-(furfural alcohol)/g-C3N4 nanocomposites with enhanced charge carrier separation for photocatalytic H2 evolution, Carbon 115 (2017) 486–492.

[28] J. Wang, L. Tang, G. Zeng, Y. Deng, Y. Liu, L. Wang, Y. Zhou, Z. Guo, J. Wang, C. Zhang, Atomic scale g-C3N4/Bi2WO6 2D/2D heterojunction with enhanced photocatalytic degradation of ibuprofen under visible light irradiation, Appl. Catal. B: Environ. 209 (2017) 285–294.

[29] L. Yuan, M.-Q. Yang, Y.-J. Xu, Tuning the surface charge of graphene for self-assembly synthesis of a SnNb2O6 nanosheet–graphene (2D-2D) nanocomposite with enhanced visible light photoactivity, Nanoscale 6 (2014) 6335–6345.

[30] M. Wang, M. Shen, L. Zhang, J. Tian, X. Jin, Y. Zhou, J. Shi, 2D-2D MnO2/g-C3N4 heterojunction photocatalyst: in-situ synthesis and enhanced CO2 reduction activity, Carbon 120 (2017) 23–31.

[31] Q. Xu, B. Zhu, C. Jiang, B. Cheng, J. Yu, Constructing 2D/2D Fe2O3/g-C3N4 direct Z-scheme photocatalysts with enhanced H2 generation performance, Sol. Rrl 2 (2018) 1800006.

[32] L. Xie, J. Ni, B. Tang, G. He, H. Chen, A self-assembled 2D/2D-type protonated carbon nitride-modified graphene oxide nanocomposite with improved photocatalytic activity, Appl. Surf. Sci. 434 (2018) 456–463.

[33] S. Tonda, S. Kumar, M. Bhardwaj, P. Yadav, S. Ogale, g-C3N4/NiAl-LDH 2D/2D hybrid heterojunction for high-performance photocatalytic reduction of CO2 into renewable fuels, ACS Appl. Mater. Inter. 10 (2018) 2667–2678.

[34] Y. Ao, K. Wang, P. Wang, C. Wang, J. Hou, Synthesis of novel 2D-2D pn heterojunction BiOBr/La2Ti2O7 composite photocatalyst with enhanced photocatalytic performance under both UV and visible light irradiation, Appl. Catal. B: Environ. 194 (2016) 157–168.

[35] L. Ye, J. Fu, Z. Xu, R. Yuan, Z. Li, Facile one-pot solvothermal method to synthesize sheet-on-sheet reduced graphene oxide (RGO)/ZnIn2S4 nanocomposites with superior photocatalytic performance, ACS Appl. Mater. Inter. 6 (2014) 3483–3490.

[36] W.-J. Ong, L.-L. Tan, S.-P. Chai, S.-T. Yong, A.R. Mohamed, Surface charge modification via protonation of graphitic carbon nitride (g-C3N4) for electrostatic self-assembly construction of 2D/2D reduced graphene oxide (rGO)/g-C3N4 nanostructures toward enhanced photocatalytic reduction of carbon dioxide to methane, Nano Energy 13 (2015) 757–770.

[37] H. Yang, R. Cao, P. Sun, X. Deng, S. Zhang, X. Xu, Highly dispersed and noble metal-free MPX (M = Ni, Co, Fe) coupled with g-C3N4 nanosheets as 0D/2D photocatalysts for hydrogen evolution, Appl. Surf. Sci. 458 (2018) 893–902.

[38] Z. Zhang, J. Huang, M. Zhang, Q. Yuan, B. Dong, Ultrathin hexagonal SnS2 nanosheets coupled with g-C3N4 nanosheets as 2D/2D heterojunction photocatalysts

toward high photocatalytic activity, Appl. Catal. B: Environ. 163 (2015) 298–305.

[39] S. Zhang, J. Li, X. Wang, Y. Huang, M. Zeng, J. Xu, Rationally designed 1D Ag@ AgVO3 nanowire/graphene/protonated gC3N4 nanosheet heterojunctions for enhanced photocatalysis via electrostatic self-assembly and photochemical reduction methods, J. Mater. Chem. A 3 (2015) 10119–10126.

[40] L. Wei, Y. Chen, Y. Lin, H. Wu, R. Yuan, Z. Li, MoS2 as non-noble-metal co-catalyst for photocatalytic hydrogen evolution over hexagonal ZnIn2S4 under visible light irradiations, Appl. Catal. B: Environ. 144 (2014) 521–527.

[41] D. Zeng, L. Xiao, W.-J. Ong, P. Wu, H. Zheng, Y. Chen, D.-L. Peng, Hierarchical ZnIn2S4/MoSe2 nanoarchitectures for efficient noble-metal-free photocatalytic hydrogen evolution under visible light, ChemSusChem 10 (2017) 4624–4631.

[42] Q. Wang, W. Wang, L. Zhong, D. Liu, X. Cao, F. Cui, Oxygen vacancy-rich 2D/2D BiOCl-g-C3N4 ultrathin heterostructure nanosheets for enhanced visible-light-driven photocatalytic activity in environmental remediation, Appl. Catal. B: Environ. 220 (2018) 290–302.

[43] D.A. Giannakoudakis, N.A. Travlou, J. Secor, T.J. Bandosz, Oxidized g-C3N4 nanospheres as catalytically photoactive linkers in MOF/g-C3N4 composite of hierarchical pore structure, Small 13 (2017) 1601758.

[44] L. Shi, L. Yang, W. Zhou, Y. Liu, L. Yin, X. Hai, H. Song, J. Ye, Photoassisted construction of holey defective g-C3N4 photocatalysts for efficient visible-light-driven H2O2 production, Small 14 (2018) 1703142.

[45] M. Karimi-Nazarabad, E.K. Goharshadi, Highly efficient photocatalytic and photoelectrocatalytic activity of solar light driven WO3/g-C3N4 nanocomposite, Sol. Energy Mater. Sol. C 160 (2017) 484–493.

[46] Y. Li, Y. Xue, J. Tian, X. Song, X. Zhang, X. Wang, H. Cui, Silver oxide decorated graphitic carbon nitride for the realization of photocatalytic degradation over the full solar spectrum: from UV to NIR region, Sol. Energy Mater. Sol. C 168 (2017) 100–111.

[47] X. Shi, M. Fujitsuka, S. Kim, T. Majima, Faster electron injection and more active sites for efficient photocatalytic H2 evolution in g-C3N4/MoS2 hybrid, Small 14 (2018) 1703277.

[48] H. Gao, H. Yang, J. Xu, S. Zhang, J. Li, Strongly coupled g-C3N4 nanosheets-Co3O4 quantum dots as 2D/0D heterostructure composite for peroxymonosulfate activation, Small 14 (2018) 1801353.

[49] Y. Xia, Q. Li, K. Lv, D. Tang, M. Li, Superiority of graphene over carbon analogs for enhanced photocatalytic H2-production activity of ZnIn2S4, Appl. Catal. B: Environ. 206 (2017) 344–352.

[50] S. Zhang, X. Liu, C. Liu, S. Luo, L. Wang, T. Cai, Y. Zeng, J. Yuan, W. Dong, Y. Pei, Y. Liu, MoS2 quantum dot growth induced by S vacancies in a ZnIn2S4 monolayer: atomic-level heterostructure for photocatalytic hydrogen production, ACS Nano 12 (2018) 751–758.

[51] Y.-J. Yuan, J.-R. Tu, Z.-J. Ye, D.-Q. Chen, B. Hu, Y.-W. Huang, T.-T. Chen, D.-P. Cao, Z.-T. Yu, Z.-G. Zou, MoS2-graphene/ZnIn2S4hierarchical microarchitectures with an electron transport bridge between light-harvesting semiconductor and cocatalyst: a highly efficient photocatalyst for solar hydrogen generation, Appl. Catal. B: Environ. 188 (2016) 13–22.

[52] S. Zhang, H. Yang, H. Gao, R. Cao, J. Huang, X. Xu, One-pot synthesis of CdS irregular nanospheres hybridized with oxygen-incorporated defect-rich MoS2 ultrathin nanosheets for efficient photocatalytic hydrogen evolution, ACS Appl. Mater. Inter. 9 (2017) 23635–23646.

[53] H. Gao, R. Cao, X. Xu, S. Zhang, H. Yongshun, H. Yang, X. Deng, J. Li, Construction of dual defect mediated Z-scheme photocatalysts for enhanced photocatalytic hydrogen evolution, Appl. Catal. B: Environ. 245 (2019) 399–409.

[54] Y. Zhu, L. Wang, Y. Liu, L. Shao, X. Xia, In-situ hydrogenation engineering of ZnIn2S4 for promoted visible-light water splitting, Appl. Catal. B: Environ. 241 (2019) 483–490.

[55] S. Zhang, H. Yang, H. Huang, H. Gao, X. Wang, R. Cao, J. Li, X. Xu, X. Wang, Unexpected ultrafast and high adsorption capacity of oxygen vacancy-rich WOx/C nanowire networks for aqueous Pb2+ and methylene blue removal, J. Mater. Chem. A 5 (2017) 15913–15922.

[56] S. Zhang, H. Gao, Y. Huang, X. Wang, T. Hayat, J. Li, X. Xu, X. Wang, Ultrathin g-C3N4 nanosheets coupled with amorphous Cu-doped FeOOH nanoclusters as 2D/0D heterogeneous catalysts for water remediation, Environ. Sci. Nano 5 (2018) 1179–1190.

[57] H. Bian, Y. Ji, J. Yan, P. Li, L. Li, Y. Li, S. Liu, In situ synthesis of few-layered g-C3N4 with vertically aligned MoS2 loading for boosting solar-to-hydrogen generation, Small 14 (2018) 1703003.